Chronopotentiometric approach in scanning electrochemical cell microscopy: minimizing surface change upon landing

Zhou, Hu; Li, Yuanjiao; Morel, Alban; Mauzeroll, Janine

Publisher's version / Version de l'éditeur:

https://doi.org/10.1021/acsami.5c02198

ACS Applied Materials & Interfaces, 17, 20, pp. 30233-30240, 2025-05-12

Chronopotentiometric Approach in Scanning Electrochemical Cell Microscopy: Minimizing Surface Change upon Landing

Hu Zhou,[†] Yuanjiao Li,[†] Alban Morel,[*,‡] and Janine Mauzeroll[*,†]

[†]*Department of Chemistry, McGill University, Montreal, QC H3A 0B8, Canada*

[‡]*Automotive and Surface Transportation Research Centre, Division of Transportation and Manufacturing, National Research Council Canada, Aluminum Technology Center, Saguenay, QC G7H 8C3, Canada*

E-mail: alban.morel@cnrc-nrc.gc.ca; janine.mauzeroll@mcgill.ca

Abstract

In single-channel scanning electrochemical cell microscopy, the pipette is usually approached to the sample surface by applying a potential while simultaneously monitoring the current. The movement of the pipette is halted once the transient current reaches a set threshold, indicating the droplet-surface contact. In corrosion study, it has been reported that the transient current can affect subsequent electrochemical measurements by polarizing the metal surface. Herein, a chronopotentiometric approach method, which involves applying a constant zero current and simultaneously monitoring the potential, is compared with the typical chronoamperometric approach method. The surface change is minimized when using the chronoampperometric approach method as confirmed by extracting the charge transfer resistance from electrochemical impedance spectroscopy in scanning electrochemical cell microscopy. This

study demonstrates that the chronopotentiometric approach method with a zero approach current alleviates the risks of changing the surface of interest. It highlights the capability of scanning electrochemcial cell microscopy to investigate the properties of pristine surfaces, thereby extending the potential applications of this technique.

Introduction

Scanning electrochemical cell microscopy (SECCM) allows for the correlation of surface reactivity with microstructure on various surfaces.[1–5] A meniscus formed at the tip of a pipette filled with electrolyte solution acts as an electrochemical cell for high-resolution imaging when it makes contact with the surface. The spatial resolution depends on the size of the opening of the pulled pipette, which can be adjusted from nanoscale to microscale.[6,7] Among the various applications of SECCM, including electrocatalysis,[8–10] electrodeposition and patterning,[11,12] and characterization of two-dimensional materials,[13–15] it has been extended into corrosion science since 2019.[16–27]

In most of the applications to corrosion study, SECCM is typically operated by bringing a single-channel pipette into contact with the metal surface while applying a potential and simultaneously monitoring the current until it reaches a certain threshold. The transient current used to trigger the stop of pipette movement is large on conductive substrates.[28,29] For passive metals, large currents lead to oxide layer damage, which is undesirable as it alters the pristine state of the surface.[30] In the measurements on aluminum alloy using SECCM, the negative approach potential causes variations in the corrosion potential E_{corr} in open circuit potential (OCP) and potentiodynamic polarization (PDP) measurements, as well as the frequency of pitting.[25] Approaching in a controlled-current mode, which was introduced by the Unwin group,[31,32] is expected to offer solutions to this problem. Controlled-current methods are primarily used in electroplating and electrocatalysis, where fine control of the reaction rate is desired.[33,34] If the current is controlled at a low magnitude (e.g., 0 A) during the SECCM approach, surface changes that affect the corrosion measurements can

be minimized.

In this work, we systematically compare the controlled-current (chronopotentiometric) approach and the controlled-potential (chronoamperometric) approach used in SECCM to study the corrosion of aluminum. The footprints of the landings on pure Al of the two approach methods are presented to demonstrate their different meniscus-surface contact state. For example, with the chronoamperometric approach, the pipette tip physically contacts the pure Al surface, whereas with the chronopotentiometric approach, only the droplet contacts the pure Al surface. The effect of the contact state on the OCP and PDP results obtained by SECCM is analyzed separately from the effect of surface change. Subsequently, the surface change caused by the large transient current in the chronoamperometric method are verified by comparing the charge transfer resistance with that obtained from the chronopotentiometric method using SECCM-electrochemical impedance spectroscopy (EIS). This study then extends the application of the two methods to measurements on aluminum alloy (AA), where significantly less metastable pitting behavior is observed using the chronopotentiometric approach. It demonstrates the ability of the chronopotentiometric approach method to capture the electrochemical properties of the pristine metal surface without causing significant changes during the approach process.

Experimental Section

Chemicals and Materials. Sodium chloride (NaCl, 99.0% purity) was purchased from Sigma-Aldrich. The pure Al foils (99.999% as rolled, GoodFellow) with a thickness of 2 mm and a size of 2.5 × 2.5 cm were purchased from Delta Scientific Laboratory Products. The AA7075-T6 samples were provided by the NRC (National Research Council Canada, Saguenay), which were then cut into 2 x 2 cm pieces of 2 mm thickness. The NaCl solution (3.5 wt%, pH = 7) was prepared with Milli-Q water (18.2 MΩ cm resistivity at 25 °C, Millipore).

Sample preparation. The pure Al was ground successively with 320, 1200, 4000 grit SiC papers (Struers, Canada) until the final step of polishing using a colloidal silica suspension (OP-S, 0.25 µm, Struers, Canada) with a MD Chem cloth pad (Struers, Canada). The polished sample surface was sonicated in water, ethanol and acetone for 10 min to remove the residuals of silica particles, before it was dried in air.

Instrumentation. The SECCM experiments were performed with an ElProScan 1 system (bipotentiostat model PG618, HEKA, Germany) in a Faraday cage on a vibration isolation table (Micro 60 Halcyonics Active Vibration Isolation Platform, Novascan, Ames IA, USA). All electrochemical measurements were performed in a 3-electrode system, with a saturated calomel electrode (SCE) (CHI 150, CH Instruments) as the reference electrode (RE) and a platinum wire (GoodFellow) as the counter electrode (CE).

Oil-immersed SECCM. The micropipettes with a 2 µm diameter opening were fabricated from quartz glass capillaries (Sutter Instrument, Navato, CA) with dimension of (o.d./i.d.) 1.0/0.3 mm using a CO_2-laser puller. The pulling parameters are: heat = 585, filament = 2, velocity = 30, delay = 130, pull = 30. The micropipette was filled with NaCl solution and then connected to a syringe with a PVC tube (inner diameter 0.76 mm). The SCE and Pt wire were both immersed in the same NaCl solution in the syringe. To prevent the droplet at the pipette tip from evaporating, a layer of mineral oil was added onto the sample surface. The approach process is explicitly described and criticized in the following part. Once a spot on the surface was wetted by the droplet, electrochemical tests involving a 60 s OCP measurement followed by a PDP measurement (scan rate: 100 mV/s, potential range: -1.3 V to -0.3 V) or an EIS measurement (frequency range: 200 kHz to 1 Hz, amplitude: 10 mV) were performed. After the measurements, the sample surface was rinsed with acetone to remove the oil and imaged using a VHX-7000 KEYENCE optical microscope to capture the landing footprints.

Figure 1: (a) The scheme of oil-immersed SECCM setup. In chronoamperometric (CA) mode, a potential -E_{app} = 2.5 V is applied to the CE and the output current is measured on the metal surface. In chronopotentiometric (CP) mode, a current i_{app} = 0 A is applied to the CE and the output potential is measured between the metal surface and RE. (b) The approach curves of CA approach (blue) and CP approach (red).

Results and Discussion

Working Principles of Chronoamperometric Approach and Chronopotentiometric Approach. The scheme of the oil-immersed SECCM setup is depicted in Figure 1a (not to scale). In chronoamperometric (CA) mode, the approach potential E_{app} = -2.5 V vs. SCE, which means a 2.5 V was applied to the CE as the pipette moved towards the metal surface. When the droplet meniscus protruding from the micropipette tip was away from the surface, the current output i_{output} measured on the surface remained at the background noise level (around 0.4 pA oscillation, see Figure 1b blue curve). As soon as the meniscus made contact with the surface, the ionic contact led to a transient increase in current beyond the break criterion (1 pA), stopping further approach of the micropipette.

In chronopotentiometric (CP) mode, an approach current i_{app} = 0 A was applied to the CE. In the absence of meniscus-surface contact, the output potential E_{output} was in an undefined state by the design of the amplifier, and it gradually drifted towards the electronics saturation limit (-5 V for HEKA PG618 potentiostat). Upon establishment of contact and closure of the electrochemical cell, E_{output} jumped from the lower limit potential to the

open circuit potential of the metal in the electrolyte solution (Figure 1b red curve). The significant change in E_{output} surpassed the break criterion (1 V), halting the micropipette approach. In both CA or CP approach, the SECCM experiment is performed in a hopping mode, necessitating approach of the droplet onto the surface for each experimental spot.

From the experimental perspective, the current threshold magnitude in the CA approach is typically close to the noise level, making it susceptible to environmental vibrations, which can easily produce a current exceeding the threshold and result in false landings where the droplet-surface contact is not made. Whereas, in the CP approach, the potential changes are much larger, in the order of volts, making the trigger very clear and not limited by instrument noise or precision. Thus, a break criterion significantly bigger than the noise can be set to reduce the occurrence of false landings.

Figure 2: (a) The footprints of two approach methods on pure Al. Pipette indentation is observed with the CA approach, but not with the CP approach. (b) There is a discrepancy between the E_{output} obtained by the two approach methods. The median of E_{output} is -1.65 V with the CP approach, and -1.05 V with the CA approach. (c) The current magnitudes of five PDP curves obtained by the two methods exhibit significant differences. The data variance for the CP approach is considerably smaller than that of the CA approach.

Distinct Electrochemical Results Are Obtained by CP and CA Approach Methods. The two approach methods were compared by measuring the same pure Al surface across 8 rows of 11 landings, alternating between CP and CA methods. Remarkably distinct contact patterns were observed from the landing footprints. The footprints of CA approach (outlined in blue in Figure 2a) shows concave circles with diameter of about 2 μm similar to the tip size, indicative of pipette indentation upon contact. Conversely, the

footprints of CP approach (outlined in red in Figure 2a) are scarcely discernible under microscopic observation. However, the subsequent PDP results in Figure 2c indicate that reactions occur in the droplet cell, suggesting that the droplet contacts the surface. The indentation observed with CA approach can be attributed to the presence of an insulating oxide film. When the droplet meniscus encounters this oxide film, the transient current is limited due to its high resistance. However, as the micropipette continues its descent to generate a current surpassing the break criterion, it physically damages the oxide film upon crashing onto the surface. In contrast, with CP approach, potential changes occur within the instrument response time upon droplet-surface contact as it is not dependant on reaction kinetics, avoiding surface indentation. The two approach methods yield notably different electrochemical results. The histogram depicting the distribution of E_{corr}(OCP) is presented in Figure 2b. The median E_{corr}(OCP) value obtained by the CP approach is -1.65 V, whereas the median E_{corr}(OCP) value obtained by the CA approach is -1.05 V. Figure 2c shows five representative PDP curves obtained by the CP and CA approach methods, respectively (overlapped in the CP approach). Notably, the magnitude of currents observed in subsequent PDP curves using the CP approach is lower compared to those obtained by the CA approach, which will be explained in the next section. Additionally, the variance among PDP curves obtained by the CP approach is significantly smaller than those obtained via the CA approach.

In the CA approach the substantial transient current density generated upon droplet-surface contact will induce damages the existing oxide film. This surface change due to cathodic polarization during CA approach, together with pipette indentation shown in Figure 2a, causes the disparity in electrochemical results between the two approach methods.

The Meniscus-Droplet Contact State Only Affects Cathodic Reactivity. To isolate and analyze the individual influences and emphasize the contact state, an alternative approach protocol was compared with normal CP approach, involving a downward movement of the z-piezo by 0.5 µm after the CP approach. This protocol artificially creates pipette

Figure 3: (a) An alternative approach protocol aiming to artificially create pipette indentation by moving the z-piezo downward by 0.5 µm after the CP approach was compared with normal CP approach. (b) E_{corr}(OCP) obtained by the alternative approach is similar to that by the CA approach. (c) The PDP curves obtained by the alternative approach show overlapped anodic branch with the CP approach, but the cathodic currents are larger.

indentation without introducing transient cathodic polarization, as illustrated in Figure 3a. Three representative OCP curves of each approach protocol are shown in Figure 3b. The E_{corr}(OCP) values at 60 s for the alternative approach protocol fall within the range of E_{corr}(OCP) distribution obtained by CA approach shown in Figure 2b. It suggests that the difference in E_{corr}(OCP) between the CP and CA approach methods originates from the different contact state. Specifically, when pipette indentation occurs, the oxide layer is disrupted at the edge of the pipette tip, such that more O_2 can diffuse from the oil to surface. Consequently, a larger cathodic current is generated, which positively shifts the E_{corr}(OCP) based on the mixed potential theory.[35] The increase in cathodic currents due to pipette indentation is corroborated by the subsequent PDP curves shown in Figure 3c. Conversely, the overlapping of anodic branches observed in both blue and red curves from -0.9 V to -0.3 V indicates that the anodic currents remain constant with the CP approach, irrespective of pipette or droplet contact.

The SECCM-EIS Verifies the Surface Change Due to Cathodic Polarization During CA Approach.

Due to the challenges of directly characterizing surface changes during the CA approach using microscopic techniques, an indirect method is employed, which involves measuring the charge transfer resistance R_{ct} using EIS. R_{ct} serves as an indicator of surface resistance to the

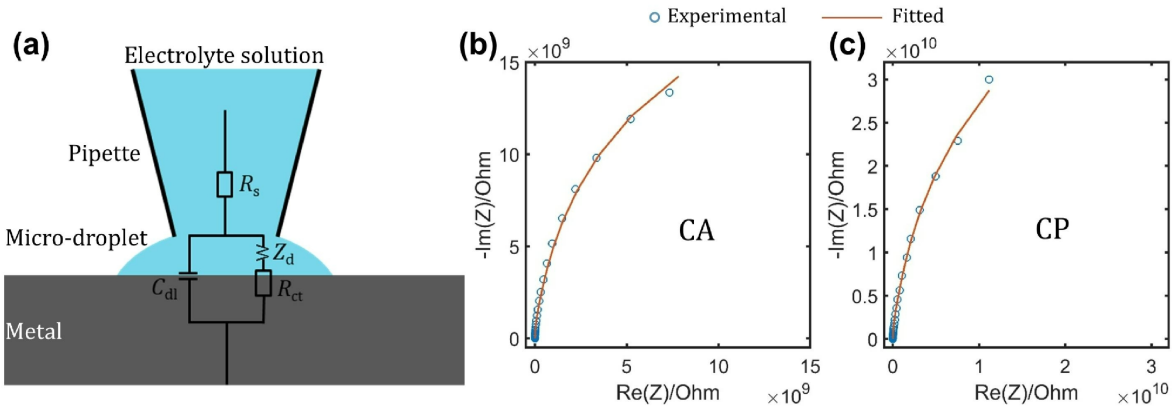

Figure 4: (a) The equivalent circuit of the micro-droplet cell consists of resistance of the solution R_{s}, capacitance of the electrical double layer at the solution/metal interface C_{dl}, resistance to the polarization at the interface R_{ct} and Warburg impedance of diffusion process Z_{d}. (b) and (c) are the Nyquist impedance plots obtained by the CA and CP approach, respectively.

polarization, with a decrease indicating potential damage to the oxide layer. Theoretically, the total impedance comprises contributions from the electrolyte solution, the pipette tip, and the metal-solution interface. However, given that the characteristic frequency of the tip is not within the frequency range employed in this study (20 kHz to 1 Hz), the impedance associated with the tip is disregarded.[36] The equivalent circuit of the micro-droplet cell is shown in Figure 4a. The impedance of the electrolyte solution is a pure resistance R_{s}. On the other hand, the impedance of the metal-solution interface consists of the charge transfer resistance in series with the Warburg impedance attributed to the diffusion of active species, denoted as Z_{d}, followed by the electrical double layer capacitance, represented in parallel as C_{dl}. Since the diffusion path is restricted by the pipette wall, semi-infinite diffusion cannot be achieved. Thus, Z_{d} is characterized by a finite length Warburg impedance expressed as follows:[37]

$$Z_{\mathrm{d}} = R_{\mathrm{d}} \frac{\tanh(\sqrt{j\tau_{\mathrm{d}}\omega})}{\sqrt{j\tau_{\mathrm{d}}\omega}} \tag{1}$$

where R_{d} is the diffusion resistance and τ_{d} is the diffusion time constant.

The Nyquist impedance obtained by the CA and CP approach methods is illustrated in

Table 1: Fitted Values of EIS circuit elements obtained by the CA and CP approach methods.

Approach Method	R_s (Ω)	C_{dl} (F)	R_{ct} (Ω)	R_d (Ω)	τ_d (s)
CA	1.02×10^{6}	6.69×10^{-12}	2.20×10^{9}	1.57×10^{10}	0.05
CP	1.10×10^{6}	4.0×10^{-12}	1.11×10^{10}	7.93×10^{10}	0.23

Figure 4b and 4c, respectively. The fitting data overlaps well with the experimental data, indicating the validity of the simplified equivalent circuit. The extracted values of the circuit elements are presented in Table 1. The R_{ct} value obtained by the CP approach (1.11×10^{10} Ω) is five times greater than that obtained by the CA approach (2.20×10^{9} Ω). This discrepancy suggests that the oxide film undergoes damage due to transient cathodic polarization with the CA approach, while the surface remains unchanged with the CP approach. The variance in PDP data can also be attributed to the consistency of R_{ct}. The R_{ct} values obtained from five experiments using the CA and CP approaches are presented in Table 2. The relative standard deviation (RSD) of R_{ct} acquired with the CA approach (136%) is significantly larger than that obtained with the CP approach (8.25%). This discrepancy arises from the fact that during each instance of the CA approach, the surface undergoes cathodic polarization of varying current magnitudes. Consequently, the CP approach yields more consistent results compared to the CA approach.

The significance of the ohmic drop in SECCM, which might be a concern due to the increased distance between the metal and the RE using the PVC tube, can be assessed from the value of R_s. Assuming the current reaches the selected current range limit (500 pA), the resulting ohmic drop is approximately 0.5 mV, which is negligible compared to the applied potential. Therefore, the ohmic drop is minimal and does not affect the accuracy of the experimental results, aligning with findings from previous studies.[24,38]

The CP Approach Method Can Reveal the Pristine Pitting Behavior of Al Alloy. The two approach methods are also compared on AA7075, known for its higher susceptibility to pitting corrosion compared to pure Al.[39,40] The potential range for PDP

Table 2: R_{ct} values of five experiments using the CA and CP approaches.

R_{ct} (Ω)	1	2	3	4	5	RSD (%)
CA	6.95×10^{9}	1.80×10^{8}	1.83×10^{9}	1.38×10^{8}	2.20×10^{9}	136
CP	1.11×10^{10}	1.10×10^{10}	9.83×10^{9}	1.01×10^{10}	9.24×10^{9}	8.25

Figure 5: (a) The anodic current map at 0 V obtained by alternating CP and CA approach on AA7075.(b) The maximum current map excluding all current smaller than 3 pA. (c) and (d) show five representative PDP curves extracted from the dashed boxes in Figure 5a. Current peaks representing metastable pitting are observed on PDP curves in (d) but not on PDP curves in (c).

measurement is from -1 V to 0 V vs. SCE. The anodic current at 0 V for each spot is extracted and presented as a scatter plot (Figure 5a), with data acquired with the CP approach outlined in red, and data acquired with the CA approach outlined in blue. Unlike pure aluminum, the magnitude of the anodic current generally does not exhibit a significant difference between the CA and CP approaches for AA7075. However, a detailed examination of the full PDP curves reveals a clear distinction between the two methods. Figure 5c and 5d present five representative PDP curves extracted from the dashed boxes in Figure 5a. Current peaks indicating the occurrence of metastable pitting corrosion followed by the repassivation of the oxide film[41] are observed exclusively on the PDP curves obtained by the CA approach method. It can be explained by the enhanced vulnerability to pitting corrosion

resulting from the hydration and increased porosity of the oxide film induced by cathodic polarization during the CA approach.[42–45] Figure 5b displays all maximum currents (i_{peak}) exceeding 3 pA. A i_{peak} value smaller than 3 pA indicates the absence of metastable pitting behavior. Apparently, there is considerably less occurrence of metastable pitting with the CP approach, although not completely absent. It implies that measurements with the CP approach unveil the genuine reactivity contrast on the surface, without interference from inconsistently stimulated hotspots introduced by the CA approach.

Figure 6: (a) A 200 µm by 200 µm E_{corr}(OCP) map measured on AA7075 by the CP approach method. (b) The maximum current map showing all currents larger than 3 pA. (c) Representative PDP curves on 4 different spots selected from the map in (b).

The CP approach method was subsequently employed to generate a large corrosion map measuring 200 µm by 200 µm (21×21 spots) on AA7075. The E_{corr}(OCP) map presented in Figure 6a confirms the successful achievement of a continuous 11 h measurement. The E_{corr}(OCP) values range from -0.85 V to -0.45 V vs. SCE, with no drifting observed throughout the entire experiment. The i_{peak} values exceeding 3 pA from the PDP measurements are extracted and plotted in Figure 6b to show the hotspots susceptible to pitting corrosion on the pristine surface. Spots 8, 9, 421 and 422 are outlined to highlight the comparison between locations exhibiting metastable pitting and those showing no pitting, which is confirmed by the full PDP curves shown in Figure 6c. The PDP curves for spots 9 and 421 exhibit a current peak indicative of oxide film breakdown and repassivation, while the PDP curves for spots 8 and 422 display nearly identical anodic current magnitudes without the metastable pitting peak. The results suggest that the CP approach enables stable and con-

sistent corrosion mapping, effectively revealing the pristine pitting behavior of the AA7075 surface.

Conclusions

A thorough comparison has been conducted between the CA and CP approach methods in SECCM. The results indicate that the CP approach can prevent pipette indentation on the pure Al surface, which is typically caused by the CA approach, thereby avoiding its impact on the cathodic current of oxygen reduction. The difference in current magnitude and variance in PDP curves between the two approach methods is shown to be unrelated to the meniscus-surface contact state, but rather due to potential surface changes caused by transient cathodic polarization during the approach. EIS has been utilized to demonstrate the minimized surface change using the CP approach method, as evidenced by the extraction of a much higher R_{ct} value compared to the CA approach. The relative standard deviation of replicated R_{ct} values indicates that the larger data variance obtained using the CA approach method is caused by the random cathodic polarization at each spot. Reduced pitting behavior has been observed on AA7075 using the CP approach method compared to the CA approach method. Therefore, the CP approach method is employed to acquire a large map of AA7075, revealing the pitting corrosion properties of the pristine alloy surface.

This work highlights the superiority of the CP approach method in SECCM, demonstrating increased accuracy and precision in PDP results. The CP approach is recommended for corrosion studies that focus on pristine surface properties, as it provides more accurate kinetic information without introducing significant changes during the approach process.

Acknowledgement

The authors acknowledge the financial support from G234176 NSERC RGPIN-2020-04609 and G248536 CQRDA/NRC. As part of a project, this work was also funded by

the NRC's METALTec industrial research group, the Centre québécois de recherche et de développement de l'aluminium (CQRDA), as well as METALTec and NPO. The authors thank Dr. Frank Wang from HEKA for his great technical supports.

References

(1) Ebejer, N.; Schnippering, M.; Colburn, A. W.; Edwards, M. A.; Unwin, P. R. Localized high resolution electrochemistry and multifunctional imaging: Scanning electrochemical cell microscopy. *Analytical chemistry* **2010**, *82*, 9141–9145.

(2) Snowden, M. E.; Guell, A. G.; Lai, S. C.; McKelvey, K.; Ebejer, N.; O'Connell, M. A.; Colburn, A. W.; Unwin, P. R. Scanning electrochemical cell microscopy: theory and experiment for quantitative high resolution spatially-resolved voltammetry and simultaneous ion-conductance measurements. *Analytical chemistry* **2012**, *84*, 2483–2491.

(3) Ebejer, N.; Güell, A. G.; Lai, S. C.; McKelvey, K.; Snowden, M. E.; Unwin, P. R. Scanning electrochemical cell microscopy: a versatile technique for nanoscale electrochemistry and functional imaging. *Annual review of analytical chemistry* **2013**, *6*, 329–351.

(4) Takahashi, Y.; Kumatani, A.; Shiku, H.; Matsue, T. Scanning probe microscopy for nanoscale electrochemical imaging. *Analytical chemistry* **2017**, *89*, 342–357.

(5) Wahab, O. J.; Kang, M.; Unwin, P. R. Scanning electrochemical cell microscopy: A natural technique for single entity electrochemistry. *Current Opinion in Electrochemistry* **2020**, *22*, 120–128.

(6) Bentley, C. L.; Kang, M.; Unwin, P. R. Scanning electrochemical cell microscopy: new perspectives on electrode processes in action. *Current Opinion in Electrochemistry* **2017**, *6*, 23–30.

(7) Jayamaha, G.; Maleki, M.; Bentley, C. L.; Kang, M. Practical guidelines for the use of scanning electrochemical cell microscopy (SECCM). *Analyst* **2024**,

(8) Bentley, C. L.; Kang, M.; Unwin, P. R. Nanoscale structure dynamics within electrocatalytic materials. *Journal of the American Chemical Society* **2017**, *139*, 16813–16821.

(9) Choi, M.; Siepser, N. P.; Jeong, S.; Wang, Y.; Jagdale, G.; Ye, X.; Baker, L. A. Probing single-particle electrocatalytic activity at facet-controlled gold nanocrystals. *Nano letters* **2020**, *20*, 1233–1239.

(10) Mariano, R. G.; McKelvey, K.; White, H. S.; Kanan, M. W. Selective increase in CO2 electroreduction activity at grain-boundary surface terminations. *Science* **2017**, *358*, 1187–1192.

(11) Tarnev, T.; Cychy, S.; Andronescu, C.; Muhler, M.; Schuhmann, W.; Chen, Y.-T. A universal nano-capillary based method of catalyst immobilization for liquid-cell transmission electron microscopy. *Angewandte Chemie International Edition* **2020**, *59*, 5586–5590.

(12) McKelvey, K.; O'Connell, M. A.; Unwin, P. R. Meniscus confined fabrication of multidimensional conducting polymer nanostructures with scanning electrochemical cell microscopy (SECCM). *Chemical communications* **2013**, *49*, 2986–2988.

(13) Liu, D.-Q.; Tao, B.; Ruan, H.-C.; Bentley, C. L.; Unwin, P. R. Metal support effects in electrocatalysis at hexagonal boron nitride. *Chemical communications* **2019**, *55*, 628–631.

(14) Takahashi, Y.; Kobayashi, Y.; Wang, Z.; Ito, Y.; Ota, M.; Ida, H.; Kumatani, A.; Miyazawa, K.; Fujita, T.; Shiku, H.; others High-Resolution Electrochemical Mapping of the Hydrogen Evolution Reaction on Transition-Metal Dichalcogenide Nanosheets. *Angewandte Chemie International Edition* **2020**, *59*, 3601–3608.

(15) Strange, L. E.; Yadav, J.; Garg, S.; Shinde, P. S.; Hill, J. W.; Hill, C. M.; Kung, P.; Pan, S. Investigating the redox properties of two-dimensional MoS2 using photoluminescence spectroelectrochemistry and scanning electrochemical cell microscopy. *The Journal of Physical Chemistry Letters* **2020**, *11*, 3488–3494.

(16) Yule, L. C.; Bentley, C. L.; West, G.; Shollock, B. A.; Unwin, P. R. Scanning electrochemical cell microscopy: A versatile method for highly localised corrosion related measurements on metal surfaces. *Electrochimica Acta* **2019**, *298*, 80–88.

(17) Yule, L. C.; Shkirskiy, V.; Aarons, J.; West, G.; Bentley, C. L.; Shollock, B. A.; Unwin, P. R. Nanoscale active sites for the hydrogen evolution reaction on low carbon steel. *The Journal of Physical Chemistry C* **2019**, *123*, 24146–24155.

(18) Li, Y.; Morel, A.; Gallant, D.; Mauzeroll, J. Oil-immersed scanning micropipette contact method enabling long-term corrosion mapping. *Analytical Chemistry* **2020**, *92*, 12415–12422.

(19) Liu, S.; Shi, M.; Zhou, Y.; Li, R.; Xie, Z.; Hu, D.; Zhang, M.; Hu, G. Scanning electrochemical cell microscopy: a powerful method to study the intergranular corrosions of archaeological silver artifacts. *Journal of Cultural Heritage* **2020**, *46*, 176–183.

(20) Shkirskiy, V.; Yule, L.; Daviddi, E.; Bentley, C.; Aarons, J.; West, G.; Unwin, P. Nanoscale scanning electrochemical cell microscopy and correlative surface structural analysis to map anodic and cathodic reactions on polycrystalline Zn in acid media. *Journal of The Electrochemical Society* **2020**, *167*, 041507.

(21) Yule, L. C.; Shkirskiy, V.; Aarons, J.; West, G.; Shollock, B. A.; Bentley, C. L.; Unwin, P. R. Nanoscale electrochemical visualization of grain-dependent anodic iron dissolution from low carbon steel. *Electrochimica Acta* **2020**, *332*, 135267.

(22) Daviddi, E.; Shkirskiy, V.; Kirkman, P. M.; Robin, M. P.; Bentley, C. L.; Unwin, P. R. Nanoscale electrochemistry in a copper/aqueous/oil three-phase system: surface structure–activity-corrosion potential relationships. *Chemical Science* **2021**, *12*, 3055–3069.

(23) Li, Y.; Morel, A.; Gallant, D.; Mauzeroll, J. Ag+ interference from Ag/AgCl wire quasi-reference counter electrode inducing corrosion potential shift in an oil-immersed scanning micropipette contact method measurement. *Analytical Chemistry* **2021**, *93*, 9657–9662.

(24) Li, Y.; Morel, A.; Gallant, D.; Mauzeroll, J. Correlating corrosion to surface grain orientations of polycrystalline aluminum alloy by scanning electrochemical cell microscopy. *ACS Applied Materials & Interfaces* **2022**, *14*, 47230–47236.

(25) Li, Y.; Morel, A.; Gallant, D.; Mauzeroll, J. Controlling surface contact, oxygen transport, and pitting of surface oxide via single-channel scanning electrochemical cell microscopy. *Analytical Chemistry* **2022**, *94*, 14603–14610.

(26) Lai, Z.; Liu, M.; Bi, P.; Huang, F.; Jin, Y. Perspectives on Corrosion Studies Using Scanning Electrochemical Cell Microscopy: Challenges and Opportunities. *Analytical Chemistry* **2023**, *95*, 15833–15850.

(27) Sun, X.; Liu, S.; Hu, P.; Sun, S.; Xie, Z.; Hu, G.; Hu, D.; Zhang, M. Microscale Corrosion Inhibition Behavior of Four Corrosion Inhibitors (BTA, MBI, MBT, and MBO) on Archeological Silver Artifacts Based on Scanning Electrochemical Cell Microscopy. *Analytical Chemistry* **2023**, *95*, 14686–14694.

(28) Takahashi, Y.; Kumatani, A.; Munakata, H.; Inomata, H.; Ito, K.; Ino, K.; Shiku, H.; Unwin, P. R.; Korchev, Y. E.; Kanamura, K.; others Nanoscale visualization of redox activity at lithium-ion battery cathodes. *Nature communications* **2014**, *5*, 5450.

(29) Kumatani, A.; Miura, C.; Kuramochi, H.; Ohto, T.; Wakisaka, M.; Nagata, Y.; Ida, H.; Takahashi, Y.; Hu, K.; Jeong, S.; others Chemical dopants on edge of holey graphene accelerate electrochemical hydrogen evolution reaction. *Advanced Science* **2019**, *6*, 1900119.

(30) Takahashi, H.; Fujiwara, K.; Seo, M. The cathodic polarization of aluminum covered with anodic oxide films in a neutral borate solution—II. Film breakdown and pit formation. *Corrosion science* **1994**, *36*, 689–705.

(31) Daviddi, E.; Gonos, K. L.; Colburn, A. W.; Bentley, C. L.; Unwin, P. R. Scanning Electrochemical Cell Microscopy (SECCM) Chronopotentiometry: Development and Applications in Electroanalysis and Electrocatalysis. *Analytical Chemistry* **2019**, *91*, 9229–9237.

(32) Daviddi, E.; Shkirskiy, V.; Kirkman, P. M.; Robin, M. P.; Bentley, C. L.; Unwin, P. R. Nanoscale electrochemistry in a copper/aqueous/oil three-phase system: surface structure–activity-corrosion potential relationships. *Chem. Sci.* **2021**, *12*, 3055–3069.

(33) Martínez-Paredes, G.; González-García, M. B.; Costa-García, A. In situ electrochemical generation of gold nanostructured screen-printed carbon electrodes. Application to the detection of lead underpotential deposition. *Electrochimica Acta* **2009**, *54*, 4801–4808.

(34) Benck, J. D.; Hellstern, T. R.; Kibsgaard, J.; Chakthranont, P.; Jaramillo, T. F. Catalyzing the Hydrogen Evolution Reaction (HER) with Molybdenum Sulfide Nanomaterials. *ACS Catalysis* **2014**, *4*, 3957–3971.

(35) Frankel, G. S. In *Active Protective Coatings: New-Generation Coatings for Metals*; Hughes, A. E., Mol, J. M., Zheludkevich, M. L., Buchheit, R. G., Eds.; Springer Netherlands: Dordrecht, 2016; pp 17–32.

(36) Cheng, L.; Jin, R.; Jiang, D.; Zhuang, J.; Liao, X.; Zheng, Q. Scanning Electrochemical Cell Microscopy Platform with Local Electrochemical Impedance Spectroscopy. *Analytical Chemistry* **2021**, *93*, 16401–16408.

(37) Lasia, A. In *Modern Aspects of Electrochemistry*; Conway, B. E., Bockris, J. O., White, R. E., Eds.; Springer US: Boston, MA, 2002; pp 143–248.

(38) Blount, B.; Juarez, G.; Wang, Y.; Ren, H. iR drop in scanning electrochemical cell microscopy. *Faraday Discuss.* **2022**, *233*, 149–162.

(39) Szklarska-Smialowska, Z. Pitting corrosion of aluminum. *Corrosion Science* **1999**, *41*, 1743–1767.

(40) Szklarska-Smialowska, Z. Insight into the pitting corrosion behavior of aluminum alloys. *Corrosion Science* **1992**, *33*, 1193–1202.

(41) Tian, W.; Du, N.; Li, S.; Chen, S.; Wu, Q. Metastable pitting corrosion of 304 stainless steel in 3.5.

(42) Lin, C.; Porter, M. D.; Hebert, K. R. Surface Films Produced by Cathodic Polarization of Aluminum. *Journal of The Electrochemical Society* **1994**, *141*, 96.

(43) Moon, S.-M.; Pyun, S.-I. The corrosion of pure aluminium during cathodic polarization in aqueous solutions. *Corrosion Science* **1997**, *39*, 399–408.

(44) Gudić, S.; Radošević, J.; Smoljko, I.; Kliškić, M. Cathodic breakdown of anodic oxide film on Al and Al–Sn alloys in NaCl solution. *Electrochimica Acta* **2005**, *50*, 5624–5632.

(45) Lin, C.; Hebert, K. R. The Effect of Prior Cathodic Polarization on the Initiation of Pitting on Aluminum. **1990**, *137*, 3723.

TOC Graphic

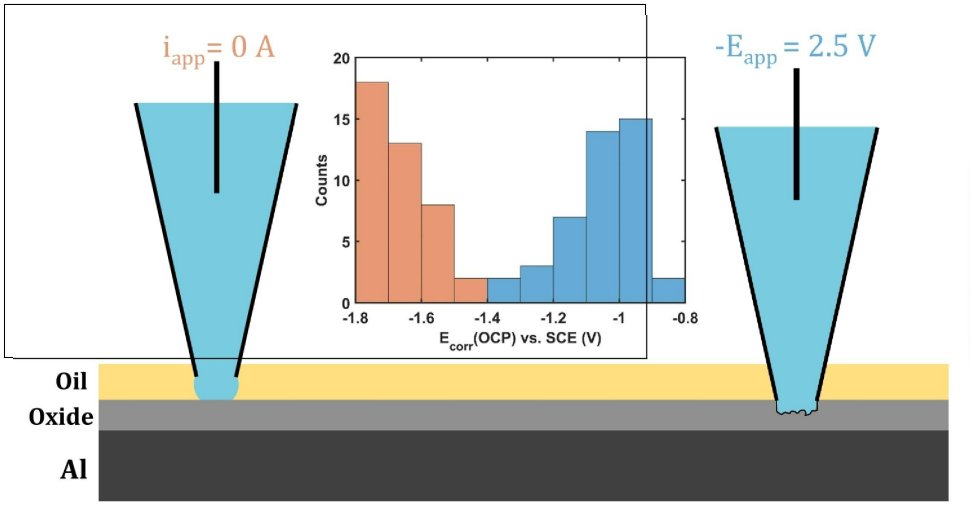
i_{app} = 0 A
$-E_{app}$ = 2.5 V
20
15
10
5
0
Counts
-1.8
-1.6
-1.4
-1.2
-1
-0.8
E_{corr}(OCP) vs. SCE (V)
Oil
Oxide
Al